

Article

Single-Image Multi-Parametric Representation of Optical Properties through Encodings to the HSV Color Space

Verónica Mieites ^{1,2,*} , José A. Gutiérrez-Gutiérrez ^{1,2}, José M. López-Higuera ^{1,2,3} and Olga M. Conde ^{1,2,3,*} 

¹ Grupo de Ingeniería Fotónica, Universidad de Cantabria, Avenida Los Castros S/N, 39006 Santander, Spain; josealberto.gutierrez@unican.es (J.A.G.-G.); miguel.lopezhiguera@unican.es (J.M.L.-H.)

² Instituto de Investigación Sanitaria Valdecilla (IDIVAL), Calle Cardenal Herrera Oria, 39011 Santander, Spain

³ Centro de Investigación Biomédica en Red. Bioingeniería, Biomateriales y Nanomedicina (CIBER-BBN), C. de Melchor Fernández Almagro, 3, 28029 Madrid, Spain

* Correspondence: veronica.mieites@unican.es (V.M.); olga.conde@unican.es (O.M.C.)

Abstract: The visualization of 2D clinical data often relies on color-coded images, but different colormaps can introduce cognitive biases, impacting result interpretation. Moreover, when using color for diagnosis with multiple biomarkers, the application of distinct colormaps for each parameter can hinder comparisons. Our aim was to introduce a visualization technique that utilizes the hue (H), saturation (S), and value (V) in a single image to convey multi-parametric data on various optical properties in an effective manner. To achieve this, we conducted a study involving two datasets, one comprising multi-modality measurements of the human aorta and the other featuring multiple parameters of dystrophic mice muscles. Through this analysis, we determined that H is best suited to emphasize differences related to pathology, while V highlights high-spatial-resolution data disparities, and color alterations effectively indicate changes in chemical component concentrations. Furthermore, encoding structural information as S and V within the same image assists in pinpointing the specific locations of these variations. In cases where all data are of a high resolution, H remains the optimal indicator of pathology, ensuring results' interpretability. This approach simplifies the selection of an appropriate colormap and enhances the ability to grasp a sample's characteristics at a single glance.

Keywords: HSV color space; optical properties; structure; chemical composition; optical coherence tomography; hyperspectral imaging; diagnostic maps; attenuation coefficient; birefringence



Citation: Mieites, V.; Gutiérrez-Gutiérrez, J.A.; López-Higuera, J.M.; Conde, O.M. Single-Image Multi-Parametric Representation of Optical Properties through Encodings to the HSV Color Space. *Appl. Sci.* **2024**, *14*, 155. <https://doi.org/10.3390/app14010155>

Academic Editors: Valentina Notarstefano, Elisabetta Giorgini, Hugh J. Byrne and Fiona Lyng

Received: 23 November 2023

Revised: 15 December 2023

Accepted: 20 December 2023

Published: 23 December 2023



Copyright: © 2023 by the authors. Licensee MDPI, Basel, Switzerland. This article is an open access article distributed under the terms and conditions of the Creative Commons Attribution (CC BY) license (<https://creativecommons.org/licenses/by/4.0/>).

1. Introduction

Data visualization is at the core of data sharing and clinical assessment, allowing for the easy interpretation of numerical results by end users, such as clinicians. When discussing 2D sets of data, researchers usually represent them as false-color images that are created by mapping some parameter to a color scale, referred to as colormaps. These colormaps and their construction can be defined in terms of certain luminance/lightness, chroma/hue, and saturation/value properties [1], leading to a wide range of options to choose from, which results in a lack of consensus on the best colormap for the representation of different types of data [2].

Color and vision perception are mainly cognitive processes, so the use of different colormaps will lead to different, sometimes more accurate, interpretations of the same results [3]. There are multiple articles that explore the variation in the explainability of the results in terms of different perception biases [4–6], such as the dark-is-more bias, where darker colors are believed to represent greater values, or the hotspot-is-more bias, where the localized accumulation of data points is interpreted as greater quantities, even if the color of the hotspot itself is not darker than that of the surrounding ones [4,7]. Further interpretation can be derived from analyzing the influence of colormap properties independently of each other. Recent experiments found that the structures in data (shapes and patterns) are best viewed in luminance variations, since the human capability to resolve

chroma variations is worse than that of luminance [8]. These claims lead to the assertion that a rapidly changing (high spatial frequency/high resolution) dataset would benefit from the use of colormaps with perceptually uniform luminance, while a lower-resolution dataset could be better represented from a chroma-variation-first colormap to exploit the dark- or hotspot-is-more biases.

Given the intricate relationship between perception biases and data visualization, numerous studies have explored the impact of different colormaps on the visualization and representation of identical 2D data [9], the creation of task-customized colormaps [10–13], as well as the best way to build a color-based representation [14–17]. Conventional colormaps, featuring diverse spectral arrangements, have the potential to elicit varied perceptual responses due to the interplay of color and luminance gradients. Researchers have examined how these colormap properties influence critical factors such as data clarity, interpretability, and the prevention of misinterpretations [18–21]. The choice of color scale can significantly affect the perceived magnitude and patterns within a dataset, potentially leading to disparities in comprehension. Moreover, the exploration of diverging, sequential, or categorical colormaps adds complexity to the investigation, as each type may excel or fail in different contexts [22].

When dealing with the optical properties of clinical data, more often than not, samples are analyzed with several imaging modalities, which can help to better understand the physiology of different pathologies. However, such imaging devices may yield data with different spatial properties. In such cases, one could provide numerous false-color images for the various parameters, each of which would be better viewed in a different colormap according to their characteristics. Nonetheless, evaluating multiple color scales for the same sample may complicate the interpretability of the dataset or even worsen it [23].

Some imaging modalities, such as polarization imaging, combine different parameters using the hue–saturation–value (HSV) color space, assigning different optical properties to each component in terms of the existing relationship between the physical parameters and the interpretation of the H, S, and V coordinates, but the correction of such parameters to enable better visualization is based on the user input [24]. Others use the addition of color as a semi-transparent overlay on a grayscale image, combined with further manipulation in the H channel to enhance the clinical differences, without variations in S and V [25]. A similar process was used to represent speckle variance over optical coherence tomography images, but the assignment of data to HSV was performed in terms of noise intensity [26].

Overall, having multiple maps for different optical properties is useful but, in some environments where rapid decision making is crucial, having an additional single image that contains all the necessary information might yield faster results. Inspired by the approaches taken in polarization imaging research, we propose a method of encoding the optical properties of biological tissue in the three components of the HSV color space by specifically choosing the parameters based on their visualization properties. This approach allows for the combination of high- and low-resolution data into a single image that conveys more information and possesses better explainability than its individual components, while still being easily interpretable and avoiding the need to select an optimal colormap for each one. The assignment to HSV makes use of the three colorimetric components and is designed to provide a clinical interpretation of the samples through color, with the most clinically relevant optical property being assigned to the H component. The S and V components are chosen based on the data with the highest resolution and spatial features, taking advantage of the human ability to recognize luminance variations as structural differences. The proposed enhancement of HSV is done automatically, taking into account the range of all possible values in a dataset, and thus using only one HSV legend shared by all the samples in it. With this work, the aim is to continue expanding the research on colormaps and color perception in the realm of clinical imaging.

2. Materials and Methods

2.1. Datasets

The proposed method can be applied to any combination of two or three different magnitudes that have complementary information about the data. However, since the focus of our research lies in the optical properties of biological tissues, we recovered two datasets to test the applicability of the proposed visualization methodology in two case studies: one composed of human samples of aortic tissue and another of dystrophic mice muscles.

For the aorta dataset, we used two ex vivo samples of the human ascending thoracic aorta: a healthy one as a control (AR26, healthy transplant donor) and a pathological aneurysmatic one (AR21, with presence of atheroma plaques). Aortas were measured with optical coherence tomography (OCT) to evaluate their structures, and their composition was studied with hyperspectral imaging (HSI). From the OCT measurements, the overall attenuation coefficient (μ_t) was derived by comparing its response to that of a reference material, as proposed by Scolaro et al. [27]. On the other hand, the model proposed by Jacques et al. [28] was used to obtain an estimation for the elastin, water, and lipids, using the spectra measured by Sekar et al. [29,30] as a reference. Specifically, we used the fraction of elastin c_e as a marker of an aortic aneurysm.

The muscle dataset contained three dystrophic mice muscles of differently aged mice (control, 1-month-old dystrophic and 3-month-old dystrophic mice). The muscles were measured and treated as described in our previous work [31], where we obtained the μ_t with the same technique as for the aortas, but also their birefringence (Δn) by measuring their polarization responses with polarization-sensitive OCT (PS-OCT). The method proposed to calculate the Δn was first described by Chin et al. in [32]. Since both OCT modalities (regular and PS) are captured with the same device, Δn and μ_t have the same spatial resolution and are implicitly co-registered.

These optical properties, namely μ_t , Δn and c_e , can be used to characterize the samples from the structural and chemical points of view. Specifically, μ_t is a measurement of how quickly light decays inside the sample; therefore, smaller μ_t values indicate that light can travel to further tissue depths without being completely attenuated. Given that μ_t is dominated by scattering, its value can be an indicator of the cell size, and therefore of the tissue morphology, which might change with different tissue structures. Additionally, Δn is affected by tissue anisotropy, with highly anisotropic structures (e.g., collagen/fiber bundles) yielding higher values of Δn . The number of tissue chromophores (collagen, elastin, fat), and specifically c_e , at different points on the sample can complement the information given by μ_t and Δn , since many structural alterations are caused by the sub- or overexpression of some tissue components, such as elastin. Combining structural-/chemical-based information can be extremely useful for the understanding of multiple pathologies.

The derivation of the attenuation coefficient μ_t and the birefringence Δn and the chromophore modeling are beyond the scope of this work and have been thoroughly described in the literature [27–32]. The measurement procedure, on the other hand, does depend on the type of sample and, specifically, on its size. Our OCT system has an FOV of $10 \times 10 \text{ mm}^2$, which makes the imaging of the entire aortas impossible in a single measurement. To maintain a spatial reference between measurements and instrumental systems, a 9-by-9 square grid with squares of $10 \times 110 \text{ mm}^2$ was designed and 3D-printed for the posterior mosaicking of the aorta measurements. We refer to each of the squares in the grid as a region of interest (ROI). The PS-OCT measurement of the mice muscles was performed with the same OCT device, but, in this case, only one measurement was needed to obtain an image of the whole muscle due to their reduced footprint. Aorta HSI was performed with a rotating-mirror-based system [33] that captured wavelengths between 1000 nm and 1700 nm, which is the range in which the most relevant chromophores of tissue are detectable. The field of view was much wider than for the OCT, namely $15 \times 15 \text{ cm}^2$; therefore, the whole aorta was imaged in a single HSI data cube by keeping the squared grid for co-registration with the OCT data.

2.2. Color Transformation

In the HSV color space, the hue (H) indicates the color portrayed in a cyclic fashion, ranging from red to green to blue and back to red. Usually, it is represented as an angle between 0° and 360° , but it can be remapped to the $[0, 1]$ range [34]. The cyclic nature of H can be avoided by cropping the H values to $[0.3, 1]$, which would remove the first third of colors corresponding to red–orange–yellow while maintaining the last red corresponding to the highest H values. The saturation (S) of a color represents its distance from its grayscale equivalent; therefore, highly saturated images will provide vibrant, colored images, while saturation values close to zero will yield a fully grayscale image. For each individual H and S, the value (V) represents its shade or tint. For example, a vibrant red that has a fixed H and S differs from a brownish red only in its V component [35].

It is possible to use the properties of the HSV formalism to create a single representation of up to three magnitudes by assigning each of them to one coordinate of the HSV space. The proposed procedure is summarized in Algorithms 1 and 2. Our aim is to keep the transformation constant for each dataset, so the same interpretation, scale and legends can be applied for all samples in the same dataset. Since HSV magnitudes are defined in the range $[0, 1]$, we need to scale all data to this range. Let y_i be a 2D numerical map that represents some property of a sample (i). Let $Y = y_1, \dots, y_i, \dots, y_N$ be the set of y_i for all the samples in the dataset (N). Then, each y_i can be scaled to the range $[0, 1]$ while keeping the relationship between all y_i by making use of the range defined by $\min(Y)$ and $\max(Y)$ (function `ScaleData` in Algorithm 1).

Algorithm 1 Scaling and equalization functions

```

1: function SCALEDATA(data, DatasetMin, DatasetMax)
2:   ValueScaled = (data – DatasetMin)/(DatasetMax – DatasetMin)
3:   return ValueScaled
4: end function

5: function EQUALIZEHUE(data, fit, nBins)
6:   if fit then
7:     bins =  $\vec{x} \in [\min(\text{data}), \max(\text{data})]$  ▷ No. of elements: nBins
8:     histogram =  $\sum_{i=1}^n \text{DataFrequency}_i$ 
9:     CDF =  $\sum_{i=1}^n \text{histogram}_i$ 
10:   end if
11:   for all  $d \in \text{data}$  do
12:     position → find d in bins
13:     OutData = CDF(position)
14:   end for
15:   return OutData
16: end function

```

However, having data in the $[0, 1]$ range does not imply that the visualization of maps in HSV will improve the overall representation. This is of particular importance when scaling y_i with respect to Y , since the range is not defined by each y_i , but by Y . If there is one y_i with a particularly high maximum value (outliers), all of the remaining scaled y_i will have their values collapse to a small dynamic range. If this happens for the magnitude that we later assign to H, this would mean that all samples would essentially have the same “color”, resulting in insignificant visualization improvements. To compensate for this effect, histogram equalization can be performed prior to assigning Y to any HSV coordinate, as proposed in [26]. However, we propose improving the equalization process by considering the histogram of the dataset Y as a whole, as well as its cumulative distribution function (CDF), to non-linearly scale each y_i with $CDF(Y)$, so that those ranges where data are heavily compressed can be expanded to occupy the full $[0, 1]$ range. This additional equalization (function `EqualizeHue` in Algorithm 1) is applied to the magnitude representing H only, since our aim is to use color as an immediate means to distinguish between sample types.

Using a global instead of a local equalization allows for the use of only one HSV legend to compare between images. Note that histogram equalization is only necessary if the values of the dataset collapse to a small range inside the wider $[0, 1]$ range in such a way that the distribution hinders visualization (i.e., uniform H, S or V).

The magnitude-to-HSV encoding itself is easily implemented (Algorithm 2). After obtaining the limits and equalization parameters of Y , the only remaining step is to choose which y_i will be assigned to H, S or V for each sample in the dataset. Then, the HSV vector can be constructed and transformed to RGB for visualization.

The choice of which optical parameter is assigned to each HSV dimension must be carefully considered. Since our datasets comprised clinical information, we chose to assign the most clinical relevance to H, which will vary between datasets. In this case, the term “clinically relevant” refers to the ability of Y to distinguish between control and pathological samples. Specifically, we choose the Y values associated with the control samples to be displayed in green, while those of pathological ones are displayed in red. For S and V, we choose to assign those Y that have strong spatial features, since these types of variations are better visualized through luminance/value/saturation changes than through color ones.

Algorithm 2 HSV transformation. Note that this algorithm refers to the functions described in Algorithm 1

```

1: for Every sample do
2:   | Import  $\mu_t, p, c_e$ 
3: end for

4: Create a global dataset for each parameter ( $D_{\mu_t}, D_p, D_{c_e}$ )
5: Scaled( $D_{c_e}$ ) = scaleData( $D_{c_e}, \min D_{c_e}, \max D_{c_e}$ )
6: EqualizeHue(Scaled( $D_{c_e}$ ), fit = True, nBins = No. of  $D_{c_e}$  Frequencies))

7: for Each dataset  $\in (D_{\mu_t}, D_p, D_{c_e})$  do
8:   | find min and max (minD, maxD)
9: end for

10: for Every sample do
11:   | Scaled( $c_e$ ) = ScaleData( $c_e, \min D_{c_e}, \max D_{c_e}$ )
12:   |  $h \leftarrow$  EqualizeHue(Scaled( $c_e$ ), minD $c_e$ , maxD $c_e$ )
13:   |  $s \leftarrow$  ScaleData( $p, \min D_p, \max D_p$ )
14:   |  $v \leftarrow$  ScaleData( $\mu_t, \min D_{\mu_t}, \max D_{\mu_t}$ )
15:   | HSV = [h,s,v]
16:   | RGB  $\leftarrow$  color transformation from HSV to RGB
17:   | plot(RGB)
18: end for

```

3. Results

3.1. HSV for Multimodal Imaging: Degradation of Aortic Tissue

To test the combination of optical properties obtained from multiple imaging systems, we used one control and one pathological aorta sample, from which we derived the μ_t from the OCT measurements and the (adimensional, normalized) amount of elastin (c_e) as a clinical marker from the HSI-measured reflectances, with the methodology explained in Section 2. We obtained boxplots of c_e and μ_t for both samples (Figure 1a) to visualize their distributions and overlap. All distributions were different between the healthy and the pathological sample, including some chromophores not considered for representation (collagen and water). Note that the HSV space still needs a third independent magnitude to be completely defined. Initially, we took the profilometry p of the samples as obtained with OCT imaging. The final magnitude-to-HSV encoding was $c_e \rightarrow H, p \rightarrow S$ and $\mu_t \rightarrow V$.

The selected optical properties were calculated for all ROIs of our samples, yielding the images shown in Figure 1b–d. The elastin maps obtained with HSI were up-scaled to

the size of the μ_t maps via linear interpolation for the posterior matching of the H, S and V dimensions. The OCT-based maps (c) and (d) were represented as en face maps to match the visualizations given by our HSI system.

Figure 1e shows the colorimetric combination of the optical properties presented in the same figure for the pathological aorta. Given that we are now working with multiple parameters, the legend for the image should have as many dimensions as the parameters. However, we show the S = 1 plane in the portrayed legend (Figure 1f) since, at this scale, the samples are mostly flat and the profiles p have little to no effect on the final images. The difference in data structure between systems is clearly visible, especially between the c_e and μ_t maps.

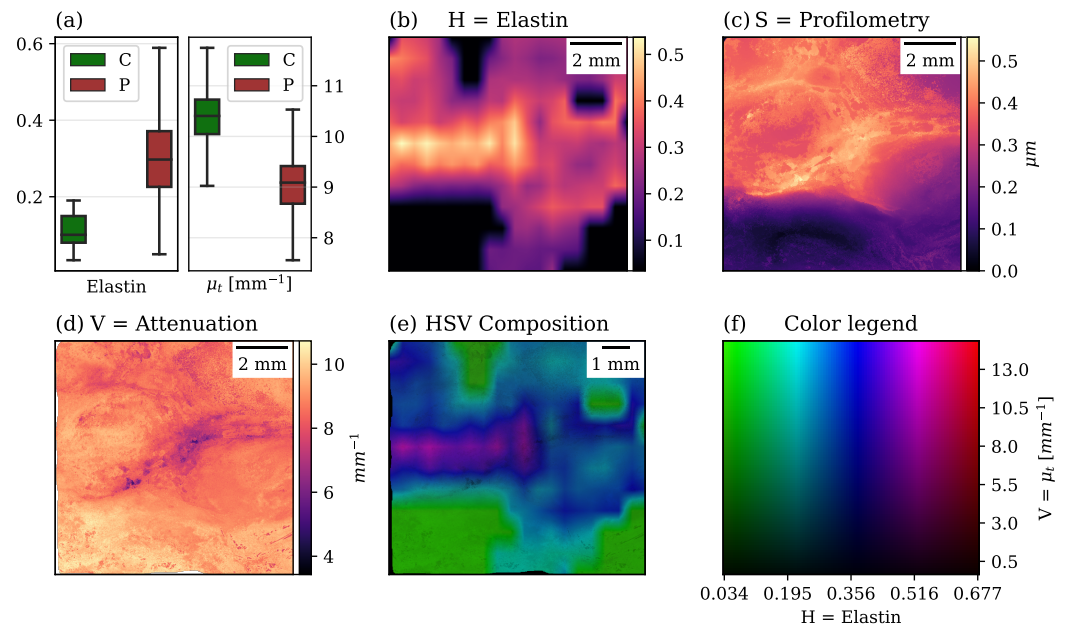


Figure 1. HSV combination of the optical properties. The clinically relevant ones are portrayed as boxplots (a) for the control (green, C) and pathological (red, P) aorta samples. Regular colormap images of c_e (b), p (c) and μ_t (d) are shown for the pathological aorta, as well as its HSV composition (e). The color legend should be three-dimensional, but, since samples at this scale were flat, only the legend for S = 1 is shown (f). There is no relevant image change for the different profilometry values for this dataset.

To explore the opportunities that this visualization method brings, we combined the HSI-derived elastin and OCT-derived μ_t in the maps shown in Figure 2 for both aortas. The color legend is the same one that was introduced in Figure 1. Color differences are immediately recognized, as well as structural variations upon closer inspection of the samples. By assigning the characteristics of the control samples to the most vibrant green (low c_e) and the pathological ones to the darkest red (high c_e), healthy regions are immediately recognized both in the control sample (Figure 2a,b) and in the pathological one (Figure 2c,d). Specifically, some heavily damaged aortic regions, marked by the red colors of c_e , are visible in the rightmost column of Figure 2d, where the darker spots indicate the reduction in μ_t . Other parts of the mosaic combine some dark signatures given by μ_t with cyan colors, indicating that there are structural changes that are not yet visible as a significant variation in the elastin content.

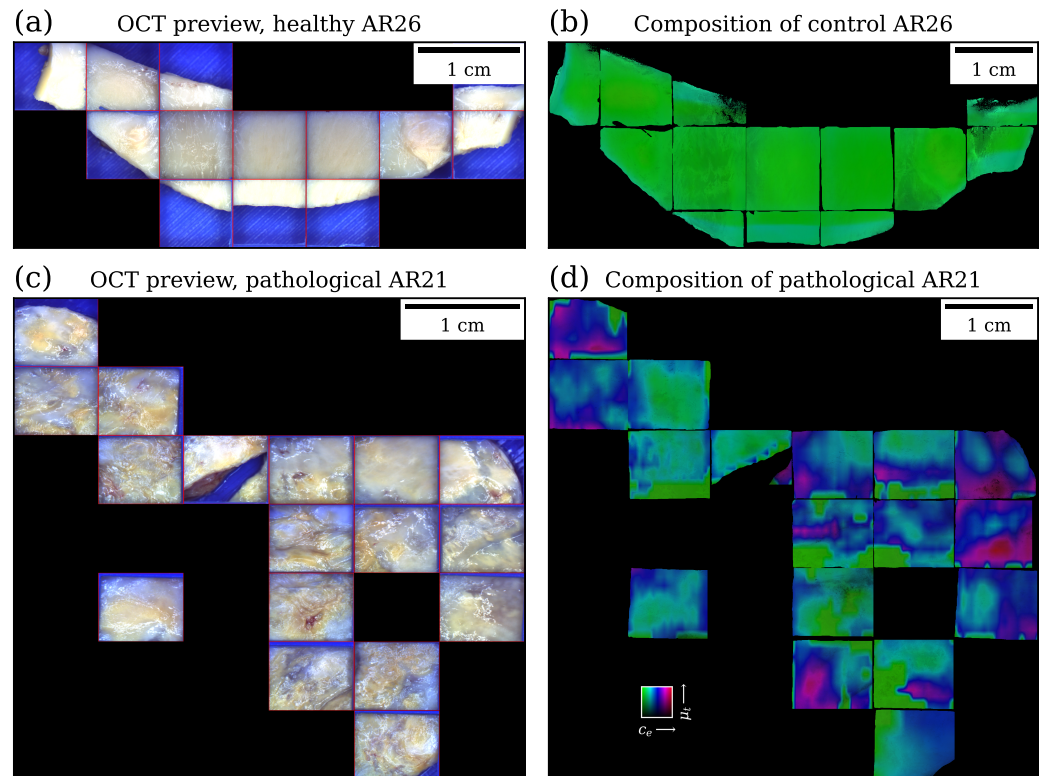


Figure 2. Application of the colorimetric combination to all ROIs of a healthy (a,b) and pathological (c,d) aorta. The color legend is the same as shown in Figure 1f, which is also provided in the lower left corner of (d). Low to high c_e values are represented from green to red, while low to high μ_t are depicted from dark to vibrant colors.

3.2. HSV for Multi-Parameter Imaging: Dystrophic Degree of Mice Samples

The application of this method is not restricted to the combination of measurements from different systems. In Figure 3, we show the transformations for the mice muscle dataset through the en face maps. The clinical marker in this case is the Δn , which indicates the level of internal structure in the samples (higher Δn means a stronger and healthier internal structure), and which was assigned to H. Again, this implies the immediate identification of healthy vs. pathological samples through color variance. Upon further exploration of the images, healthier (greener) regions on all samples, and specifically on the control one (Figure 3a), are complemented by μ_t , where the strong anisotropy indicated by the stripes defined by μ_t is also reflected by the stronger birefringence. The 1-month-old mouse sample (Figure 3a) is the complete opposite, where no spatial structure of μ_t is visible at all, which in turn yields negligible birefringence values (red), indicating the lack of internal structure and incremented muscular deterioration. Finally, the 3-month-old mouse sample (Figure 3c) lies in between the other two, with some spatial features visible and mild birefringence.

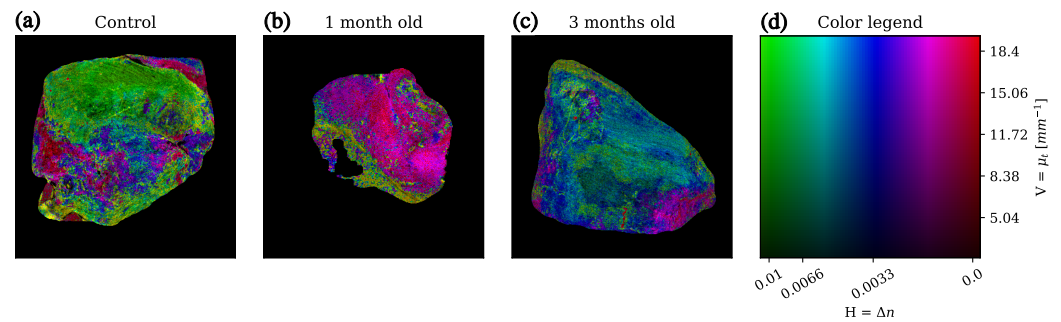


Figure 3. Application of the colorimetric combination to dystrophic mice muscles for a control mouse (a) and at different ages in the progression of the disease (b,c). In this case, we kept S and V as the profilometry and μ_t of the samples but, for the H, we used their birefringence as a clinical marker. The 2D color legend is shown in (d), where S is not shown due to the low impact of the profilometry on visualization, since the muscles were cut flat.

4. Discussion

The proposed encoding of optical properties to components of the HSV color space was applied to two use cases: the combination of parameters from different imaging modalities (healthy and pathological aorta samples) and the combination of parameters from a single system (dystrophic and control mice muscles). These measurements, taken with OCT, HSI and PS-OCT, allowed us to obtain relevant tissular optical properties for the samples, namely μ_t , c_e and Δn , respectively. All distributions were centered on different values; therefore, one could theoretically use any of them for H.

In the case of multiple-modality imaging, the OCT system provides measurements with a resolution of approximately 13 $\mu\text{m}/\text{px}$, while our HSI device yields 0.9 mm/px at the working distance for the aortas. This means that μ_t (Figure 1d) is the best for encoding V in the HSV color space since it has a much higher resolution and spatial variation than the HSI chromophores (Figure 1b). As discussed in Section 1, luminance (or, in this case, V) is the best dimension for the representation of high-resolution data due to the increased ability to detect patterns in luminance variations.

To represent S, it is necessary to use a magnitude that is independent of the other two so that the HSV space is well defined. We used the profilometry p of the sample for this task (Figure 1c), calculated as the depth of maximum intensity in the OCT images. This means that higher-resolution and better-focused regions will generate vibrant and saturated colors, while lower-resolution and out-of-focus positions will provide less saturated and, therefore, less distracting colors. Since the aortic tissue was flat, the S values were mostly constant across both samples.

For the aortas, to create the mapping of μ_t to V, we used a transformation that took the maximum and minimum of all μ_t values across the aorta dataset and re-scaled them to the 0–1 range of V. Then, this transformation was applied to each μ_t value individually. By doing so, we kept the color scale consistent across all ROIs and samples (Figure 2). The same was done for H and S, but the re-scaled, equalized range of H was 0.3–1, to avoid the cyclic nature of H, as mentioned in Section 2.

Figure 1b–d use the same perceptually uniform colormap (magma) [36], which essentially means that the selected colors have a lightness that grows linearly from 0 to 1. It is instantly clear how high-resolution data (Figure 1c,d) benefit from this type of representation, with hotspots being clearly highlighted. Discerning the elastin content variations (Figure 1b) is more difficult, due to having to distinguish between multiple shades of what is essentially the same color. On the other hand, encoding c_e as H makes it easier to pinpoint subtle variations, without losing the spatial information given by μ_t (Figure 1e).

Using the combinative visualization method allows for immediate discrimination between the two types of samples, both through the color difference between samples and also through the color uniformity (Figure 2). The co-registration with the μ_t maps helps to pinpoint the structural differences in areas with different elastin content, especially when

zooming in on one of the ROIs (Figure 1e). For example, some red/magenta areas (high c_e) coincide with darker colors (low μ_t), but, when looking at all the images, it is clear that there is no apparent visual correlation between the attenuation and elastin content. This could mean that structural changes caused by the damaging pathologies do not coincide with an increase in elastin, or that the change in the internal structure of the aortas is visible before such composition changes take place. The fact that no color is unsaturated means that all samples are flat and well focused.

In the case of multiple-parameter imaging, the process of assigning properties to HSV for the muscles (Figure 3) is identical to the case of the multiple-system imaging, with the dynamic range of Δn requiring histogram equalization as described in Section 2. We kept the S and V as the same components as for the multi-system case. For this dataset, the μ_t distributions overlapped between samples; however, structural differences are still perfectly visible after assigning them to V variations. Using high-spatial-resolution data for all three components of the HSV color space presents no issue since it allows us to still see structural and clinical differences, and the dimension and shape of the samples' profiles are comparable since we see little to no change in saturation.

For the muscles, the amount of texture provided by μ_t seems to correlate at first glance with the birefringence Δn , which is expected from healthy, anisotropic, muscular tissue. Nonetheless, additional information can still be retrieved from the combination of parameters, given that the μ_t - Δn effect is less apparent for heavily damaged samples (Figure 3b). Specifically, for the 1-month-old mouse sample, the spatial variations of μ_t are negligible; however, changes in hue reveal that the center of the muscle is more damaged (red) than its surroundings (magenta), which indicates that Δn might be a more sensitive parameter to structural changes, while μ_t is better for the enhancement of superficial features.

The aortas showed damage observable without aid that was revealed in strikingly different colors between the healthy and damaged samples (Figure 2b,d). Nevertheless, similar trends were visible in the color distribution portrayed in the muscles, where the deterioration was not visible to the naked eye (Figure 3). This shows that as long as the color marker (H, a clinically relevant parameter) has sufficiently different distributions for control and pathological samples, the proposed method is suitable to combine diagnostic and non-diagnostic information in images with an enhanced context.

Ideally, with sufficiently large datasets, this method could consider the maximum and minimum values of the studied optical parameters, as well as their probability distributions, to create a universal framework for visualization that allows for a comparison between multiple samples, imaging modalities or devices. Similar studies of this type of color encoding to different areas have already been implemented [24–26], which indicates that this approach might be applicable to any form of dataset. However, any HSV or color encoding, including the one presented in this work, has the evident drawback of not being colorblind-friendly. In such cases, an attempt to optimize S and V while keeping H constant (or varying in a small range) might compensate for the lack of color resolution without compromising the pipeline of the method.

5. Conclusions

In this study, we have presented a color-space-based approach to combine optical properties in a single, information-rich visualization. The method is built upon making use of the distribution separation between two classes of clinically relevant parameters to obtain a single image that has all the advantages of its individual components at once.

We applied it to the combination of multi-modality (OCT and HSI) and multi-parametric (PS-OCT and OCT) optical properties. When most optical properties had different distributions for the different clinical cases, the choice of each parameter as a component of the HSV color space was based on the spatial frequency of the data. By doing so, we created image maps that colored the highly structured data through the low-structured information. When the resolution of the data is the same for all parameters, the selection of the transformation to HSV is only based on the differences in data distribution between clinical

categories. Since the objective is for color to be the primary label for the pathological state of the sample, we always assign to H the optical property that has distributions with the least amount of overlap between the types of samples, with the green values corresponding to those of control samples.

Finally, the proposed combination of optical properties leads to maps with enhanced information that can be useful to clinicians to detect inter- and intra-sample differences at a single glance, but they also allow for an in-depth analysis without having to re-adapt between uses of different colormaps, thus allowing for faster decision making in environments where this might be crucial.

Author Contributions: Conceptualization, V.M. and O.M.C.; methodology, V.M.; software, V.M. and J.A.G.-G.; validation, V.M., J.A.G.-G. and O.M.C.; formal analysis, V.M.; investigation, V.M.; resources, O.M.C.; data curation, V.M. and J.A.G.-G.; writing—original draft preparation, V.M.; writing—review and editing, V.M., J.A.G.-G. and O.M.C.; visualization, V.M.; supervision, O.M.C.; project administration, O.M.C.; funding acquisition, O.M.C. and J.M.L.-H. All authors have read and agreed to the published version of the manuscript.

Funding: Support for this work was provided by the projects PREVAL 21/07 (FUSIOMUSCLE) from IDIVAL; DTS22-00127 (hyPERfusioCAM) and DTS17-00055 (INTRACARDIO) funded by Instituto de Salud Carlos III (ISCIII) and co-funded by the European Union; and EQC 2019-006589-P and PID2019-107270RB-C21/AEI/10.13039/501100011033 from Ministerio de Ciencia e Innovacion and FEDER, “A way to make Europe”.

Institutional Review Board Statement: Human aorta specimens were obtained after surgical interventions at Hospital Universitario Marqués de Valdecilla (Santander, Spain) and approved by Comité Ético de Investigación Clínica de Cantabria” under the INTRACARDIO project (code number 2018.008). All animal procedures were performed according to the National Institute of Health Guidelines for the Care and Use of Laboratory Animals and were approved by the Hospital de la Santa Creu i Sant Pau Animal Ethics Committee.

Informed Consent Statement: Informed consent was obtained from all subjects involved in the study.

Data Availability Statement: Due to the datasets containing sensitive information that is used in their processing, the sharing of the code and/or data of this work may be possible upon reasonable email request to the authors.

Acknowledgments: The authors would like to thank Alejandro Ponton and Inmaculada Garcia for providing the aorta samples and also Xavier Suarez and Jordi Diaz for supplying the dystrophic muscles. The authors would also like to thank Eusebio Real and Arturo Pardo for their involvement in these measurements during their Ph.D. theses.

Conflicts of Interest: The authors declare no conflict of interest.

Abbreviations

The following abbreviations are used in this manuscript:

HSV	Hue–Saturation–Value
OCT	Optical Coherence Tomography
PS-OCT	Polarization-Sensitive OCT
HSI	Hyperspectral Imaging

References

1. Bujack, R.; Turton, T.L.; Samsel, F.; Ware, C.; Rogers, D.H.; Ahrens, J. The Good, the Bad, and the Ugly: A Theoretical Framework for the Assessment of Continuous Colormaps. *IEEE Trans. Vis. Comput. Graph.* **2018**, *24*, 923–933. [[CrossRef](#)]
2. Bernard, J.; Steiger, M.; Mittelstädt, S.; Thum, S.; Keim, D.; Kohlhammer, J. A survey and task-based quality assessment of static 2D colormaps. In *Proceedings of the Visualization and Data Analysis 2015*; Kao, D.L., Hao, M.C., Livingston, M.A., Wischgoll, T., Eds.; International Society for Optics and Photonics, SPIE: Bellingham, WA, USA, 2015; Volume 9397, p. 93970M. [[CrossRef](#)]
3. Reda, K.; Nalawade, P.; Ansah-Koi, K. Graphical Perception of Continuous Quantitative Maps: The Effects of Spatial Frequency and Colormap Design. In *Proceedings of the 2018 CHI Conference on Human Factors in Computing Systems*, Montreal, QC, Canada, 21–26 April 2018; pp. 1–2. [[CrossRef](#)]

4. Soto, A.; Schoenlein, M.A.; Schloss, K.B. More of what? Dissociating effects of conceptual and numeric mappings on interpreting colormap data visualizations. *Cogn. Res. Princ. Implic.* **2023**, *8*, 38. [[CrossRef](#)]
5. Schoenlein, M.A.; Campos, J.; Lande, K.J.; Lessard, L.; Schloss, K.B. Unifying Effects of Direct and Relational Associations for Visual Communication. *IEEE Trans. Vis. Comput. Graph.* **2023**, *29*, 385–395. [[CrossRef](#)]
6. Sibrel, S.C.; Rathore, R.; Lessard, L.; Schloss, K.B. The relation between color and spatial structure for interpreting colormap data visualizations. *J. Vis.* **2020**, *20*, 7. [[CrossRef](#)]
7. Schott, G.D. Colored Illustrations of the Brain: Some Conceptual and Contextual Issues. *Neuroscientist* **2010**, *16*, 508–518. [[CrossRef](#)]
8. Ware, C.; Stone, M.; Szafir, D.A. Rainbow Colormaps Are Not All Bad. *IEEE Comput. Graph. Appl.* **2023**, *43*, 88–93. [[CrossRef](#)] [[PubMed](#)]
9. Ware, C.; Turton, T.L.; Bujack, R.; Samsel, F.; Shrivastava, P.; Rogers, D.H. Measuring and Modeling the Feature Detection Threshold Functions of Colormaps. *IEEE Trans. Vis. Comput. Graph.* **2019**, *25*, 2777–2790. [[CrossRef](#)]
10. Pen, M. Full customization of color maps for fisheries acoustics: Visualizing every target. *Fish. Res.* **2021**, *240*, 105949. [[CrossRef](#)]
11. Barua, G.; Pingel, T.; Lim, T. Urban thermal map design considerations: Color, shading, and resolution. *Cartogr. Geogr. Inf. Sci.* **2023**. [[CrossRef](#)]
12. Zhang, Y.; Fjeld, M.; Fratarcangeli, M.; Said, A.; Zhao, S. Affective Colormap Design for Accurate Visual Comprehension in Industrial Tomography. *Sensors* **2021**, *21*, 4766. [[CrossRef](#)]
13. Knizner, K.T.; Kibbe, R.R.; Garrard, K.P.; Nunez, J.R.; Anderton, C.R.; Muddiman, D.C. On the importance of color in mass spectrometry imaging. *J. Mass Spectrom.* **2022**, *57*, e4898. [[CrossRef](#)] [[PubMed](#)]
14. Wang, X.; Yin, J.; Cheng, B.; Qin, J. Colormap optimization with data equality. *J. Vis.* **2021**, *24*, 191–203. [[CrossRef](#)]
15. Nardini, P.; Chen, M.; Böttinger, M.; Scheuermann, G.; Bujack, R. Automatic Improvement of Continuous Colormaps in Euclidean Colorspaces. *Comput. Graph. Forum* **2021**, *40*, 361–373. [[CrossRef](#)]
16. Zeng, Q.; Wang, Y.; Zhang, J.; Zhang, W.; Tu, C.; Viola, I.; Wang, Y. Data-Driven Colormap Optimization for 2D Scalar Field Visualization. In Proceedings of the 2019 IEEE Visualization Conference (VIS), Vancouver, BC, Canada, 20–25 October 2019; pp. 266–270. [[CrossRef](#)]
17. Wall, E.; Agnihotri, M.; Matzen, L.; Divis, K.; Haass, M.; Endert, A.; Stasko, J. A Heuristic Approach to Value-Driven Evaluation of Visualizations. *IEEE Trans. Vis. Comput. Graph.* **2019**, *25*, 491–500. [[CrossRef](#)] [[PubMed](#)]
18. Dasgupta, A.; Poco, J.; Rogowitz, B.; Han, K.; Bertini, E.; Silva, C.T. The Effect of Color Scales on Climate Scientists’ Objective and Subjective Performance in Spatial Data Analysis Tasks. *IEEE Trans. Vis. Comput. Graph.* **2018**, *26*, 1577–1591. [[CrossRef](#)] [[PubMed](#)]
19. Gołębiowska, I.; Çöltekin, A. What’s wrong with the rainbow? An interdisciplinary review of empirical evidence for and against the rainbow color scheme in visualizations. *ISPRS J. Photogramm. Remote Sens.* **2022**, *194*, 195–208. [[CrossRef](#)]
20. Reda, K.; Szafir, D.A. Rainbows Revisited: Modeling Effective Colormap Design for Graphical Inference. *IEEE Trans. Vis. Comput. Graph.* **2021**, *27*, 1032–1042. [[CrossRef](#)]
21. Chen, J.; Zhang, G.; Chiou, W.; Laidlaw, D.H.; Auchus, A.P. Measuring the Effects of Scalar and Spherical Colormaps on Ensembles of DMRI Tubes. *IEEE Trans. Vis. Comput. Graph.* **2020**, *26*, 2818–2833. [[CrossRef](#)]
22. Thyng, K.M. The Importance of Colormaps. *Comput. Sci. Eng.* **2020**, *22*, 96–102. [[CrossRef](#)]
23. Knippa, E.E.; Berg, E.; Richard, S.; Lin, Y.; Choudhury, K.R.; Samei, E.; Baker, J.A. Impact of Colorized Display of Mammograms on Lesion Detection. *J. Breast Imaging* **2020**, *2*, 22–28. [[CrossRef](#)]
24. Tyo, J.S.; Ratliff, B.M.; Alenin, A.S. Adapting the HSV polarization-color mapping for regions with low irradiance and high polarization. *Opt. Lett.* **2016**, *41*, 4759–4762. [[CrossRef](#)]
25. Glatz, J.; Symvoulidis, P.; Garcia-Allende, P.B.; Ntziachristos, V. Robust overlay schemes for the fusion of fluorescence and color channels in biological imaging. *J. Biomed. Opt.* **2014**, *19*, 040501. [[CrossRef](#)] [[PubMed](#)]
26. Liu, X.; Zhang, K.; Huang, Y.; Kang, J.U. Spectroscopic-speckle variance OCT for microvasculature detection and analysis. *Biomed. Opt. Express* **2011**, *2*, 2995–3009. [[CrossRef](#)] [[PubMed](#)]
27. Scolaro, L.; McLaughlin, R.A.; Klyen, B.R.; Wood, B.A.; Robbins, P.D.; Saunders, C.M.; Jacques, S.L.; Sampson, D.D. Parametric imaging of the local attenuation coefficient in human axillary lymph nodes assessed using optical coherence tomography. *Biomed. Opt. Express* **2012**, *3*, 366–379. [[CrossRef](#)]
28. Jacques, S.L. Optical properties of biological tissues: A review. *Phys. Med. Biol.* **2013**, *58*, R37–R61. [[CrossRef](#)] [[PubMed](#)]
29. Sekar, S.K.V.; Bargigia, I.; Mora, A.D.; Taroni, P.; Ruggeri, A.; Tosi, A.; Pifferi, A.; Farina, A. Diffuse optical characterization of collagen absorption from 500 to 1700 nm. *J. Biomed. Opt.* **2017**, *22*, 015006. [[CrossRef](#)] [[PubMed](#)]
30. Sekar, S.K.V.; Beh, J.S.; Farina, A.; Dalla Mora, A.; Pifferi, A.; Taroni, P. Broadband diffuse optical characterization of elastin for biomedical applications. *Biophys. Chem.* **2017**, *229*, 130–134. [[CrossRef](#)]
31. Mieites, V.; Pardo, A.; Gutiérrez-Gutiérrez, J.A.; Suárez-Calvet, X.; López-Higuera, J.M.; Díaz-Manera, J.; Conde, O.M. Colorimetric fusion of attenuation and birefringence in OCT signatures: A screening tool for evaluating muscular degradation in alpha-sarcoglycan deficit murine models. In *Optical Coherence Imaging Techniques and Imaging in Scattering Media V*; Vakoc, B.J., Wojtkowski, M., Yasuno, Y., Eds.; International Society for Optics and Photonics, SPIE: Bellingham, WA, USA, 2023; Volume 12632, p. 1263211. [[CrossRef](#)]
32. Chin, L.; Yang, X.; McLaughlin, R.A.; Noble, P.B.; Sampson, D.D. En face parametric imaging of tissue birefringence using polarization-sensitive optical coherence tomography. *J. Biomed. Opt.* **2013**, *18*, 066005. [[CrossRef](#)]

33. Gutiérrez-Gutiérrez, J.A.; Pardo, A.; Real, E.; López-Higuera, J.M.; Conde, O.M. Custom Scanning Hyperspectral Imaging System for Biomedical Applications: Modeling, Benchmarking, and Specifications. *Sensors* **2019**, *19*, 1692. [[CrossRef](#)]
34. Ibraheem, N.A.; Hasan, M.M.; Khan, R.Z.; Mishra, P.K. Understanding Color Models: A Review. *ARPN J. Sci. Technol.* **2012**, *2*, 265–275.
35. Elaw, S.; Abd-Elhafiez, W.M.; Heshmat, M. Comparison of video face detection methods using HSV, HSL and HSI color spaces. In Proceedings of the 2019 14th International Conference on Computer Engineering and Systems (ICCES), Cairo, Egypt, 17–18 December 2019; pp. 180–188.
36. Hunter, J.D. Matplotlib: A 2D graphics environment. *Comput. Sci. Eng.* **2007**, *9*, 90–95. [[CrossRef](#)]

Disclaimer/Publisher’s Note: The statements, opinions and data contained in all publications are solely those of the individual author(s) and contributor(s) and not of MDPI and/or the editor(s). MDPI and/or the editor(s) disclaim responsibility for any injury to people or property resulting from any ideas, methods, instructions or products referred to in the content.